Coordination Chemistry Reviews 253 (2009) 2387–2398

Contents lists available at ScienceDirect

Coordination Chemistry Reviews

journal homepage: www.elsevier.com/locate/ccr

Review

# STM spectroscopy of magnetic molecules

K. Petukhov[a], M.S. Alam[a], H. Rupp[a], S. Strömsdörfer[a], P. Müller[a,*], A. Scheurer[b], R.W. Saalfrank[b], J. Kortus[c], A. Postnikov[d], M. Ruben[e], L.K. Thompson[f], J.-M. Lehn[g]

[a] Department für Physik, Universität Erlangen-Nürnberg, Erwin-Rommel-Str. 1, D-91058 Erlangen, Germany
[b] Department für Chemie und Pharmazie, Universität Erlangen-Nürnberg, Germany
[c] Institut für Theoretische Physik, TU Bergakademie Freiberg, Germany
[d] Laboratoire de Physique des Milieux Denses, Université Paul Verlaine, Metz, France
[e] Institut für Nanotechnologie, Forschungszentrum Karlsruhe, Germany
[f] Department of Chemistry, Memorial University, St. John's, Newfoundland, Canada
[g] ISIS, Université Louis Pasteur, Strasbourg, France

**Contents**



ARTICLE INFO

*Article history:*
Received 31 July 2008
Accepted 18 January 2009
Available online 31 January 2009

*Keywords:*
Scanning tunneling microscopy
Current-imaging tunneling spectroscopy
Scanning tunneling spectroscopy
Single-molecule magnets
Grid-like and star-like supramolecular assemblies

ABSTRACT

We have investigated a series of magnetic supramolecular complexes involving coordinated metal ions. Using the current-imaging tunneling spectroscopy mode of a STM, we mapped isolated single molecules. By comparing with DFT calculations, we confirmed that the weakest bonds, i.e. the supramolecular coordination interactions, dominate the molecular orbitals near the Fermi-level of the molecule. Thus, STM spectroscopy can address directly the metal centers in a rather complex molecular entity. Our method allows a selective mapping of the functional units within the supramolecular architecture, even if these units are embedded into a complex set of organic ligands. We observed this behavior in all of our investigated molecules.



## 1. Introduction

Coordinated metal ions are the essential centers of chemical activity in various molecules. Beyond any chemical application, metal complexes embedded into a supramolecular entity are potential building blocks for molecular electronics [1]. Therefore, attaching the functional molecules to a substrate and investigating their behavior and properties is a primary requirement for potential applications. Progress and possibilities of metal complexes in molecular electronics have been reviewed recently, highlighting that the electronic state of metal complexes is attractive for constructing highly integrated, functional molecular components [2]. Therefore, it is natural to investigate single magnetic molecules which can be envisaged as building blocks for such type of electronics.

Scanning tunneling microscopy (STM) has been proved to be a powerful tool to study various surfaces at the atomic and molecular level. Although STM is capable of atomic resolution when imaging solid surfaces, mapping of large and complex molecules with submolecular resolution is still a difficult task. An STM image contains both geometric and electronic information about the sample in a complex way [3–5]. Even highly resolved STM topography images cannot provide information about specific features of large molecules. However, the spectroscopic possibilities of STM allow us to probe electronic states of the molecules as a function of energy within a range of few eV around the Fermi-level [6–8]. If there were subunits of the molecule exhibiting a special type of chemical bonding, STM spectroscopy would allow filtering out special features of

* Corresponding author.
*E-mail address:* phm@physik.uni-erlangen.de (P. Müller).

0010-8545/$ – see front matter © 2009 Elsevier B.V. All rights reserved.
doi:10.1016/j.ccr.2009.01.024

the species if they arise at energies well separated from the other states of the molecule.

In order to achieve a better understanding of how STM images are related to the geometric and electronic structure of the deposited complexes, we performed spatially resolved current-imaging tunneling spectroscopy (CITS) measurements. In Section 2 we describe STM and CITS techniques in detail. We restricted our measurements to the spectroscopy of occupied levels. CITS is current-imaging tunneling spectroscopy and has been developed for scanning tunneling spectroscopy (STS) of a sample surface [9,10]. The CITS technique has been applied successfully to semiconductor materials but its application to large molecules is rather difficult at ambient conditions because of mobility or instability of the molecules, etc. [11]. With our specially designed home built low-drift STM head, we successfully applied this technique to different assemblies of magnetic molecules, like [2 × 2] $Co^{II}$, [3 × 3] $Mn^{II}$ grids [12,13] and $Fe^{III}Fe_3{}^{III}$ ferric stars [14], which belong to a novel class of single-molecule magnet (SMM) materials. We discuss the STM, magnetic, and CITS investigations of grid-like and star-like supramolecular assemblies, in Sections 3 and 4, respectively.

Besides the investigations described in this paper, we have performed similar studies on $Fe_6{}^{III}$ ferric wheels [7], as well as $Cu_{20}{}^{II}$ complexes incorporated into large polyoxotungstate wheels [15]. In all cases, we were able to visualize the metal centers in the organic matrix even if they were completely hidden by the surrounding ligands.

## 2. Scanning tunneling microscopy and spectroscopy

STM is known to be a useful tool when imaging solid surfaces with atomic resolution. However, performing STM of large molecules, especially at ambient conditions, is not an easy task. Considering the van der Waals surface of rather dense assemblies of atoms, one expects a more or less featureless “spot” of a large cluster of atoms. Naturally, STM data contain both electronic and geometric information about the sample under investigation [3–5]. STS is a very useful tool to probe electronic states as a function of energy in the range of a few eV near the Fermi-level [8]. If the supramolecular clusters have energy levels within this energy range, and if these levels are well separated from other states of the molecule, STS can resolve them, and one can relate them to the building units of the supramolecular cluster. Both STM and STS techniques were applied to supramolecular assemblies formed either by 1D chains or 2D arrays or groups of free-standing single molecules.

A powerful technique, which allows studying the electronic properties of the supramolecular complexes on surfaces, is the so-called CITS. In CITS, both topological information and current–voltage (*I*–*V*) data of the object are collected at the same time [8]. At any pixel of the normal STM topography image being recorded with constant tunneling current *I*, the current control is released for a short time and *I*–*V* characteristics are measured. This results in an additional three-dimensional data set *I* (*V*, *x*, *y*), whereby *x* and *y* are the spatial positions on the surface.

The data can be displayed as a series of current images (CITS maps) representing the tunneling current *I* as a function of the lateral *x*, *y* coordinates at a given voltage *V* (see Fig. 1d, for example). At certain bias voltages, the contrast of these images changes significantly when new molecular energy levels come into play. The use of current imaging allows energy-resolved spectroscopy to be performed with spatial resolution, i.e. the density of states of the molecule can be visualized as a function of energy and position [9]. Alternatively, a series of *I*–*V* characteristics can be displayed along any trajectory across the image area (see Fig. 1a and c). This allows tracing the energy landscape of the molecule across any path of the image.

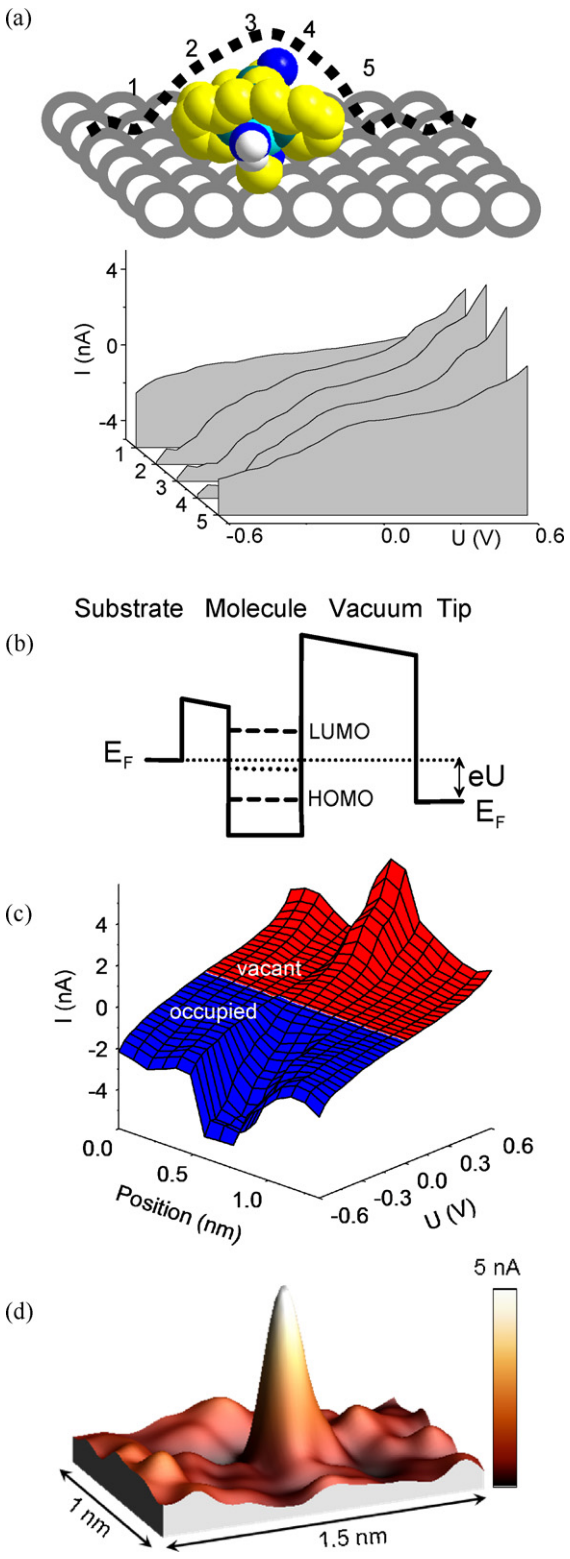


**Fig. 1.** (a) Sketch of a molecule with a metal center deposited onto a HOPG substrate (spheres). At the points labelled 1–5, IV characteristics were measured; they are shown in the lower panel. (b) Energy landscape for tunneling from a molecule deposited onto a substrate. (c) Set of IV curves measured along the dotted scan line in (a). (d) 3D current map taken at a bias voltage of 0.6 V.

In general, STM and STS techniques still remain a challenge for organic molecules, because of their mobility and instability [11]. Nevertheless, if there would be energy regions where the molecular levels exclusively result from some functional subgroups of atoms, a selective screening of parts of the molecule would be possible,

provided that the tip of the microscope could be placed in a stable way above them.

This situation is possible, for example, when a transition-metal ion is incorporated into an assembly of organic ligands via coordination bonds. Then the bonding schema of this molecular assembly shows a clear *d*-orbital character at the highest occupied states (HOMOs) and the lowest unoccupied states (LUMOs). Indeed, our DFT calculations show clearly that this is the case for all of our investigated molecules (*vide infra*). In fact, in the energy range of ±1.5 eV related to the position of the Fermi-level $E_F$, which is accessible to tunneling spectroscopy at ambient conditions, several maxima of the density of states are present. This type of spectroscopy is exemplified in Fig. 1: here, a monomer of a coordination polymer consisting of a Cu ion coordinated by an organic ligand [16] is scanned along the dotted line in Fig. 1a.

The molecule is deposited onto a (semiconducting) highly ordered pyrolytic graphite HOPG substrate. In general, for a STM measurement, there would be tunneling barriers molecule – substrate and molecule – STM tip (Fig. 1b). As the potential difference *U* is applied between tip and substrate, the position of the molecular energy levels is not fixed relative to the Fermi-levels $E_F$ of either substrate or STM tip. However, in most cases, due to a weak charge exchange between molecule and HOPG substrate, the tunneling barrier between substrate and molecule can be neglected and the molecular energy levels are fixed relative to the Fermi energy of the substrate. A negative potential of the substrate with respect to the tip (Fig. 1b) allows the Fermi-level of the tip to be scanned along the occupied molecular levels, whereas positive bias voltages probe the vacant levels (see Fig. 1c).

*I–V* data are collected at each pixel of the scan. This is exemplified for some selected points in the lower panel of Fig. 1a. From these types of data, one can build a 3D plot out of these spatially resolved *I–V* characteristics, which is depicted in Fig. 1c. When the tip is at the position of the metal ion, there are bias levels which match the resonance condition with either occupied (HOMO) or vacant (LUMO) molecular orbitals (see Fig. 1b). As a result, the tunneling current increases excessively which causes a kink in the *I–V* characteristics.

Therefore, a map of tunneling current taken at bias levels above these levels will demonstrate a clear maximum at the position of the metal ion. This procedure can be applied for any scan line of the picture thus generating a huge data set which can be evaluated in several ways as described above. As an example, a current map for a set of scan lines covering an area of 1.0 nm × 1.5 nm around the position of the molecule is shown in Fig. 1d. It shows primarily the electron density of the (vacant) *d* levels of the coordinated Cu ion up to the energy of 0.6 eV above the Fermi-level. This type of map, in principle, could also be measured directly by scanning at a certain fixed bias level. This procedure, however, is unfeasible at least under ambient conditions, since scanning at high bias levels with a current setting of several nA can cause the tip to crash into the molecule.

The investigations presented in this paper have been performed using a home-made scanning tunneling microscope. In order to keep the STM tip stable above the object, any drift effects of the microscope were minimized [16]. The microscope was fitted out with a low-current control system, commercially available from RHK Technology. The supramolecular assemblies under investigation were always put onto HOPG substrates. Firstly, low-concentration solutions (between $10^{-8}$ and $10^{-10}$ M) in water or acetonitrile were prepared out of the samples. A drop of such solution was put onto the HOPG substrate and then slowly dried. A calibration of the resolution of the tunneling tip with respect to the known interatomic distances of graphite was done in all cases before the solution was placed onto the HOPG surface. We have employed tunneling currents between 5 and 200 pA and bias voltages between ±50 and ±500 mV in our experiments. For the topography experiments we have used a frequency range between 2 and 5 Hz at a resolution of 256 × 256 points. During the CITS experiments we have reduced the scan frequency to approximately 0.3 Hz having a resolution of 128 × 128 points. Normally, for the CITS measurements we have utilized the interrupted-feedback-loop technique. The idea of such technique is based on the opening of the feedback loop in order to fix the separation between the tip and the sample and ramping of the bias voltage over the range of interest. Typically, we have varied the scan voltage in the range of −1.0 to 0.1 V relative to the tip potential having 100–140 steps in this voltage range. The tunneling resistance was set to approximately 5 GΩ. Finally, for fabrication of our tips we have employed mechanically cut Pt–Ir (90/10) wires of a diameter of 250 μm.

First-principle calculations of the electronic structure performed in the framework of density functional theory (DFT) provide a useful insight into the origin of the maxima detected in the CITS maps. The supramolecular metal-ion assemblies described here were calculated using two different DFT approaches: (i) for the grid-like [2 × 2] $Co_4^{II}$ complexes the Naval Research Laboratory Molecular Orbital Library (NRLMOL) program package was used, which is an all-electron implementation of DFT. NRLMOL combines large Gaussian orbital basis sets, numerically precise variational integration and an analytic solution of Poisson's equation in order to accurately determine the self-consistent potentials, secular matrix, total energies, and Hellmann–Feynman–Pulay forces [17]. (ii) The Mn [3 × 3] grids and the star-like supramolecular assemblies were calculated using the computer code Siesta with strictly confined numerical atom-centered basis functions [18]. A recent review dealing with DFT calculations of molecules of comparable nature as those described here can be found in Ref. [19].

Finally, we note that the DFT calculations presented here do not take into account any interactions between molecule and substrate. This can explain slight discrepancies between experiments and the theory.

## 3. Addressing the metal centers of grid-type supramolecular transition-metal assemblies

Modern supramolecular coordination chemistry provides access to an ample variety of transition-metal complexes of grid-type architecture composed in the form of two-dimensional arrays of metal ions interconnected by organic ligands. These complexes appear to be of special interest as a basis for information storage units, logic and sensing blocks [20–24]. The inherently regular network-like arrangement of metal ions within the grid-like molecules is comparable to the binary coded matrix of crossbar architectures used in conventional data storage and processing technology. Moreover, the redox [25], magnetic [23], and spin state [24] properties of such complexes have been well investigated. Like arrays of the much larger semiconductor quantum dots, grid-like assemblies might display "ion-dot" type features, if addressing could be realized within a nanometer scale, that means to realize "read" and "write" processes at the single metal-ion level. Due to their veritable geometry, flat deposition of grid-like complexes onto solid surfaces gives automatically large domains of highly ordered metal ions within a grid-type arrangement [26].

In this review we will focus on a number of square [$n \times n$] grid-like assemblies of transition-metal ions such as Co and Mn with $n \leq 5$. Transition-metal complexes of the [$n \times n$] $M^{II}$ type have been found to exhibit very interesting structural [21], optical [22], magnetic [23,24], and, in particular the [2 × 2] $Co_4^{II}$ species, remarkable electronic properties [25].

The multinuclear grid-type metal complex $[Co_4^{II}(L^1)_4](BF_4)_8$ (**1**) ($H_2L^1$ = 4,6-bis(2′,2″-bipyrid-6′-yl)-2-phenyl-pyrimidine), shown in Fig. 5a, has been thoroughly investigated by us recently [10,27].

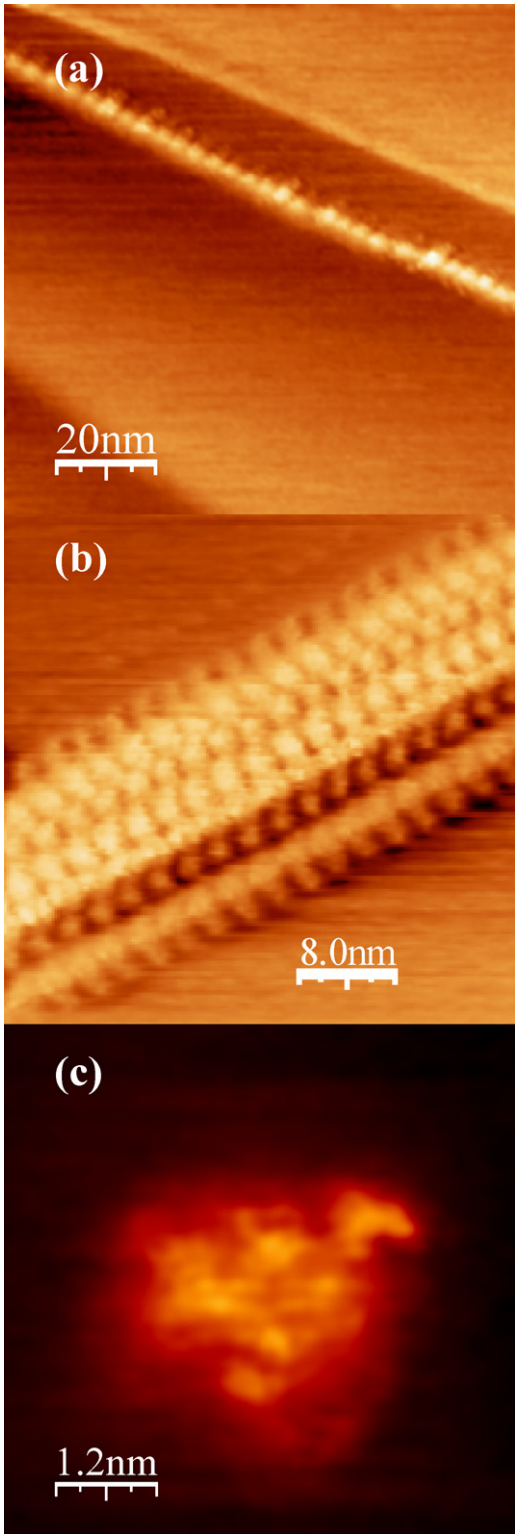


**Fig. 2.** STM images of Co [2 × 2] grid complexes **1** deposited onto a HOPG surface. (a) At low concentrations, the $[Co_4^{II}L_4^1]^{8+}$ complexes are aligned along graphite steps into 1D chains (set point current 5 pA, set point voltage 100 mV). (b) 2D crystal formed from $[Co_4^{II}L_4^1]^{8+}$ ion arrays along a graphite step (set point current 200 pA, set point voltage 100 mV). (c) An isolated molecule with submolecular resolution (set point current 200 pA, set point voltage 500 mV).

We have applied STM and STS techniques to 1D lines (Fig. 2a) and 2D clusters (Fig. 2b) as well as to isolated free-standing single molecules (Fig. 2c) of complex **1**, which was deposited onto HOPG. We should note that STM studies of densely packed monolayers of $[Co_4^{II}(L^1)_4]^{8+}$ grid complexes on HOPG have already been reported before [26,28,29]. In this paper we will concentrate mostly on the specific features of the electronic properties at the single-molecule level, therefore we will focus on isolated, free-standing molecules. Relevant work dealing with approaches towards the investigation of specific functionalities of supramolecular nanostructures at surfaces were reviewed recently [30,31].

The samples were prepared by depositing a drop of a solution of **1** in acetonitrile ($10^{-9}$ M). The molecules can aggregate in different arrangements of Co [2 × 2] complexes on the HOPG surface. After repeated scanning under relatively mild tunneling conditions, different structures can be observed, as shown in Fig. 2. When the coverage is low, the grid complexes usually get trapped along the step edges on the surface of HOPG, therefore one naturally obtains several hundred nanometers long continuous 1D chains (Fig. 2a), as well as 2D arrays of closely packed grids (Fig. 2b). Ordered 2D structures start to grow from single nucleation points. Finally, when the coverage is very low, isolated units can be found even at room temperature where thermal mobility becomes considerable, as depicted in Fig. 2c.

Fig. 2c presents a high-resolution STM image of a single [2 × 2] $Co^{II}$ block of complex **1**. The image shows a bright spot of a diameter of approximately 1.7 nm, which is in agreement with the molecular size extracted from single-crystal X-ray diffraction investigations (1.65 nm) [12]. The central bright spot is surrounded by a less

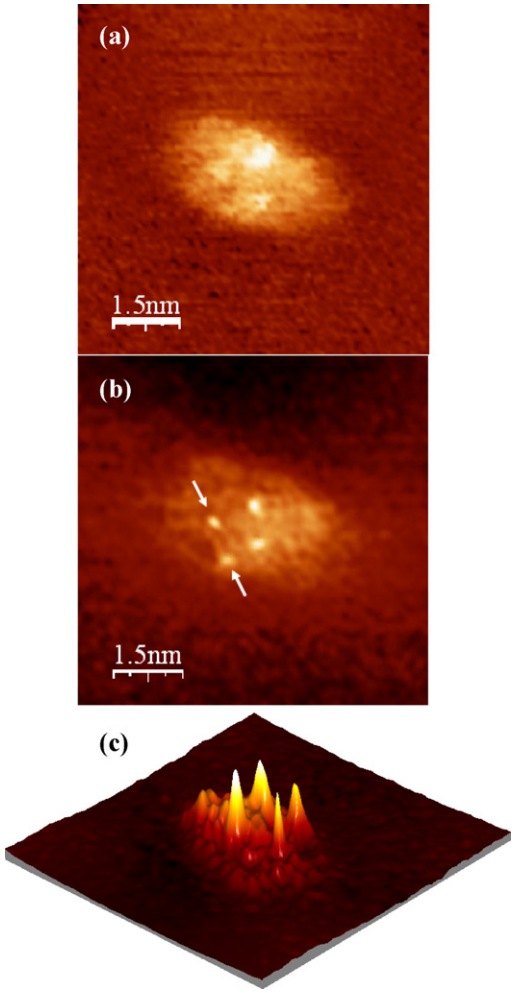


**Fig. 3.** (a) Topography map of a Co [2 × 2] grid **1**. (b) Simultaneously recorded current (CITS) image, taken at a voltage of −0.942 V. A quadratic array of bright spots can be detected at a spot-to-spot distance of approximately 0.7 nm. (c) Perspective view of a 3D representation of (b). The current scale is 8 nA.

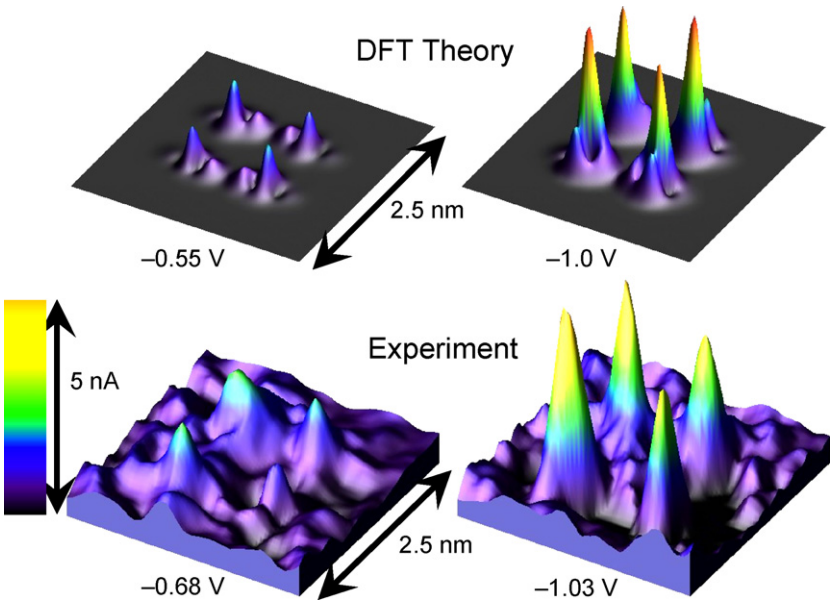


**Fig. 4.** (Top) 3D representation of calculated DFT electron density maps of **1** within an energy window between $E_F$ and $E = -0.55$ eV (left) and between $E_F$ and $E = -1.0$ eV (right); (bottom) central section of the measured CITS maps at −0.68 and −1.03 V.

defined aureole; this blur can be explained by contributions from the solvent molecules and $BF_4$ anions. More important, four even more brighter spots in a quadratic arrangement can be observed on top of the whole structure, which could correspond to the positions of the $Co^{II}$ metal ions. Besides these weak features, STM topography cannot provide any additional information on the intramolecular structure.

Therefore, in order to get further information, we have applied the CITS technique to the [2 × 2] $Co_4^{II}$ grid-like complex **1**. We have performed CITS mapping using negative sample-to-tip bias voltages, thus performing spectroscopy of the occupied levels. The results of constant current topography imaging (STM), recorded simultaneously with the CITS measurements, are presented in Fig. 3a. Fig. 3b represents a current map, obtained by CITS experiments, at a bias voltage of −0.942 V. Again, the topographic image (Fig. 3a) presents a rather featureless structure with a diameter of approximately 1.7 nm. At the same time, the CITS current map (Fig. 3b) clearly shows four bright spots, arranged in a quadratic array. These spots represent sharp peaks of the tunneling current, as shown in Fig. 3c. This picture represents a 3D view of Fig. 3b. The peaks are arranged in a square of approximately 0.7 nm × 0.7 nm, which is in perfect agreement with the distance between two neighboring cobalt ions, obtained by single-crystal X-ray diffraction investigations [12]. Since all distances between the CITS peaks correspond to the Co–Co distances in the molecule of complex **1**, we conclude that we have mapped the local maxima of the density of states at the positions of the Co ions. Under the experimental conditions, only weak additional features arising from the four bis(bipyridyl)pyrimidine ligands were observed (see Fig. 3c).

In Fig. 4 we present 3D plots of the DFT electron density maps of **1** (top), which represent the local density of states, integrated from the Fermi-level up to the bias levels shown next to the maps. The experimental data, plotted using the same color scheme, are presented in Fig. 4 (bottom) for comparison. Both the theoretical and the experimental 3D representations are shown for two different energy windows. The former window covers the energy range between $E_F$ and the HOMO (−0.55 eV); the latter energy range covers the full range between $E_F$ and −1.0 V, where all states of 3d-character should be found. As we have discussed in Section 2, the LUMO is expected to be pinned close to $E_F$ because of the high positive charge (eightfold) of complex **1**. Knowing that the DFT calculations usually underestimate band gaps, we find that the HOMO–LUMO gap is approximately 150 meV smaller than that obtained from the STM experiment. Therefore, the STM data measured at a bias of −0.7 V should be compared for consistency with DFT calculation results at a bias of −0.55 V. Indeed, the DFT electron density maps presented in Fig. 4 (top) perfectly confirm the STM experimental data, shown in Fig. 4 (bottom).

*I–V* characteristics measured along the line depicted by two arrows in Fig. 3b show a prominent increase of the tunneling current beyond the threshold voltage of about −0.6 V. This increase in *I–V* characteristics, depicted in Fig. 5b, corresponds to the presumed positions of the metal ions.

This observation can be due to the accessibility for the tunneling current of the HOMO of **1**, which has a strong Co 3d-character (Fig. 5a). Fig. 5a shows the DOS curves calculated by spin-polarized DFT with antiferromagnetic order of the Co ions. The black and the red shadings presented in Fig. 5a correspond to the two spin directions. The second peak in the calculated DOS curve of the Co 3d states matches the experimentally observed increase of the *I–V* characteristics around −1 V. Here we would like to note that the contribution of the N 2p states is negligible (Fig. 5a, lower panel). Moreover, other ligand states like C 2s, 2p or N 2s have no influence within the energy range of ±1 eV around the Fermi-level $E_F$. Therefore, we conclude that DFT calculations perfectly explain the experimental CITS maps and confirm the peak features exclusively caused by the $Co^{II}$ ions.

In order to generalize the results of the previous section, we have performed similar surface probe microscopy investigations on higher homologues of the above described [*n* × *n*] grid-like class, namely the [3 × 3] $Mn_9^{II}$ grid-like assembly $[Mn_9^{II}(L^2)_6](ClO_4)_6$ **(2)** (Fig. 6a and b) [32].

STM and CITS images of **2** adsorbed on HOPG are shown in Fig. 6c and d, respectively. Fig. 6d presents a CITS map of an isolated assembly of **2** taken at a bias of −0.73 V below the Fermi-level. It demonstrates a regular [3 × 3] grid-like array of nine tetragonally aligned sharp spots, which correspond to maxima of the tunneling current. The distances between two neighboring peaks on the CITS map shown in Fig. 6c are around 0.4 nm, which exactly correspond to the Mn–Mn distances within **2**, as measured by single-crystal X-ray diffraction [32]. The peaks perfectly reflect the regular geometrical arrangement of the metal ions in the [3 × 3]

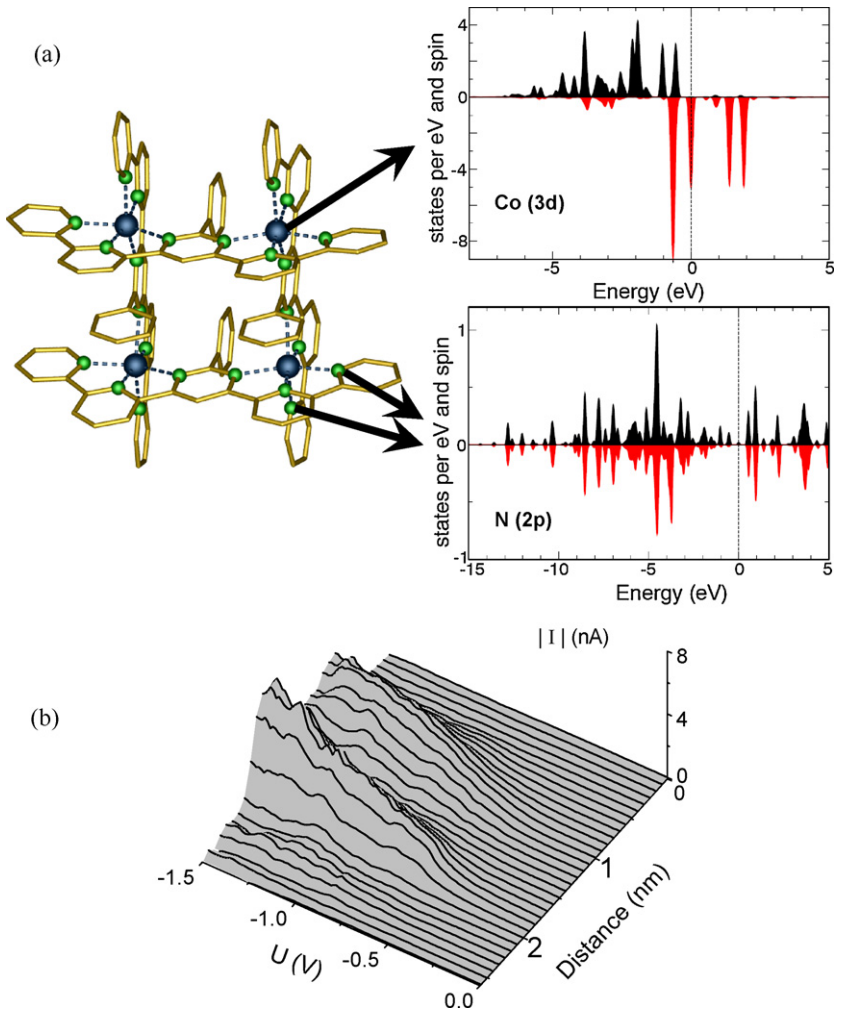


**Fig. 5.** (a) X-ray crystal structure of **1** with the local density of states (DOS) for a Co ion and for a coordinating N donor atom calculated by DFT. For better comparison both DOS curves have the same vertical scale. (b) Representation of a set of *I–V* characteristics measured along the line between two $Co^{II}$-ion corners as marked by the arrows in Fig. 3b. The background current arising from tunneling into the substrate has been subtracted.

$Mn_9^{II}$ grid-like complex (Fig. 6d). A comparison between DFT calculation and experiment shows a rather nice agreement (Fig. 6e). We would like to emphasize that no evidence of the interconnecting $(L^2)^{2-}$ ligands could be demonstrated by the CITS experiments.

These types of study have been extended systematically to Mn [4 × 4], and Mn [5 × 5] grids coordinated by tetratopic and pentatopic ligands of a type analogous to $(L^2)^{2-}$ [32]. Again the 4 × 4 and the 5 × 5 metal grids did show up nicely in the CITS measurements. We emphasize that in the case of the Mn [5 × 5] grid no X-ray structure was available. In this sense, the CITS data were able to prove, that at least one molecule was successfully synthesized.

## 4. Star-like supramolecular metal-ion assemblies (single-molecule magnets)

SMMs are a novel class of materials, where identical iso-oriented magnetic molecules are regularly assembled in large crystals. Each of the molecules is composed of coupled magnetic ions; at low temperatures the coupling is strong enough for the whole molecule to form a ground state described by a single net spin *S*. By applying a magnetic field, the net (giant) spin of the molecule can be reversed; such uniaxial magnetic bistability is demonstrated by hysteretic magnetization characteristics. Quantum tunneling of magnetization (QTM) through the magnetic anisotropy potential $E = DS^2$, where *D* is the uniaxial anisotropy parameter, is demonstrated by the presence of steps in hysteresis loops of SMMs at millikelvin temperatures [33]. At higher temperatures ($\sim E/k_BS$), thermally activated relaxation can drive the molecule from the ground spin state *S* over the barrier *E* to the opposite ground spin state $-S$. A negative uniaxial anisotropy parameter *D* of the Hamiltonian causes hysteretic magnetization characteristics even without long-range magnetic order. This effect would scale magnetic data storage down to a single-molecule level.

In this context, trigonal metal-centered $\{Fe^{III}Fe_3^{III}\}$ supramolecular assemblies such as $[Fe^{III}\{Fe^{III}(L^3)_2\}_3]$ **(3)** are among the simplest inorganic systems showing SMM behavior and therefore have been extensively studied as model system [14,34,35]. The molecular structure of these types of SMM is presented in Fig. 7b. The metal-ion assembly **3** was synthesized from the ligand *N*-methyldiethanolamine $H_2L^3$ (Fig. 7a) and ferric chloride in the presence of sodium hydride. The star-like structure, depicted in Fig. 7b, is formed by the three peripheral Fe ions which are oxo-bridged to the single central Fe ion.

The SMM properties of **3** were characterized by magnetometry and electron paramagnetic resonance (EPR) measurements. In order to find the ground spin state of the system **3** we have placed single crystals of $[Fe^{III}\{Fe^{III}(L^3)_2\}_3](3{\cdot}4\ CHCl_3)$ into a MPMS SQUID magnetometer. The magnetic susceptibility of single crystals was measured in a broad temperature range (1.8–300 K) at several magnetic field values (0.1–5.5 T). The results of these measurements are

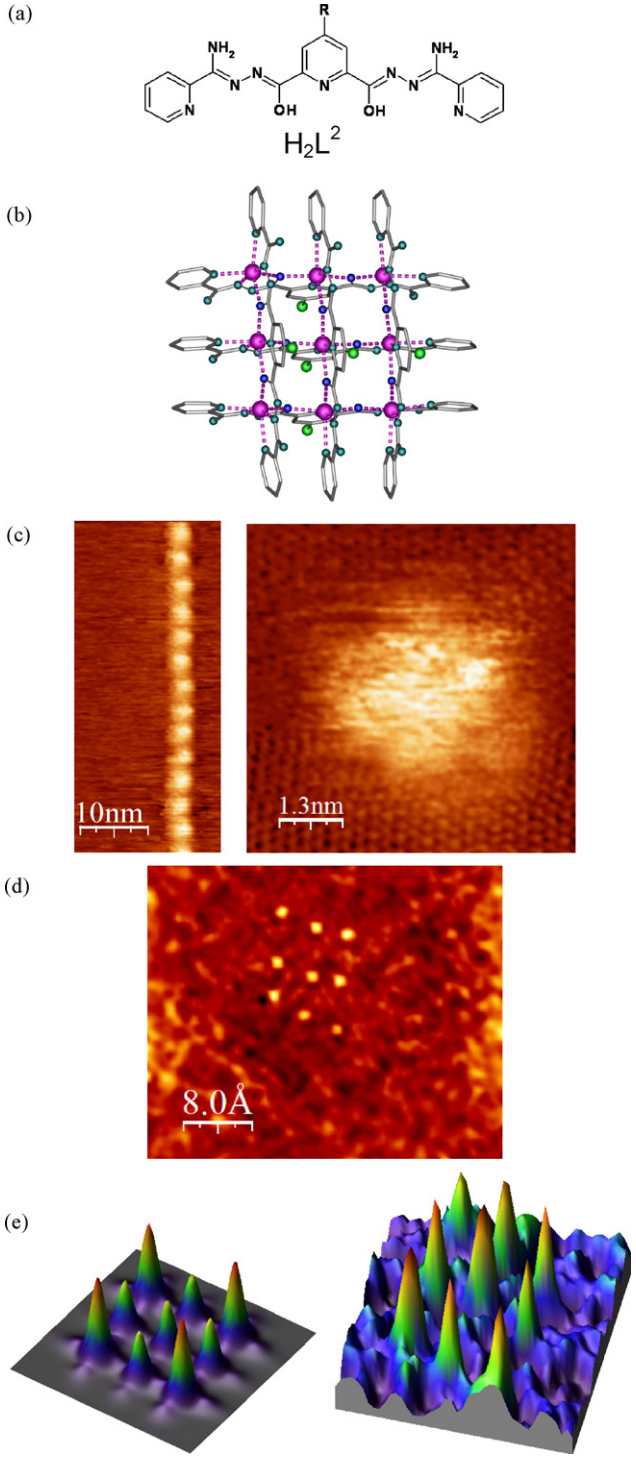


**Fig. 6.** The Mn [3 × 3] grid: (a) molecular formula of the tritopic ligand $H_2L^2$ and (b) the X-ray structure of the grid-like hexacation $[Mn_9^{II}(L^2)_6]^{6+}$. (c) Topographic STM image of a single-molecular chain (left) and a single molecule (right), showing clearly single C atoms of the HOPG substrate; (d) an experimental CITS map at −0.73 V. (e) Left: DFT electron density map of the Mn [3 × 3] grid molecule, integrated between $E_F$ and −0.9 eV. The scale is 1.7 nm × 1.7 nm. Right: 3D representation of the CITS data from (d) in the same area scale. The current scale is 1.8 nA.

presented in Fig. 8a. Moreover, as we had the possibility for two-axis rotation of the sample inside the SQUID cryostat, we have performed magnetization measurements along the crystallographic *x*-, *y*-, and *z*-axes in the magnetic field range (0–5.5 T) at the lowest operating temperature of 1.8 K.

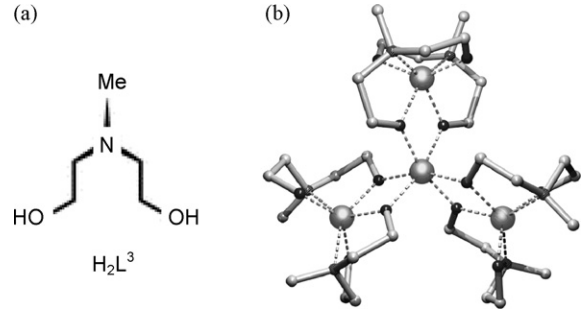


**Fig. 7.** Star-like metal-ion assembly: (a) molecular structure of ligand $H_2L^3$ and (b) representation of the X-ray structure of the star-like complex $[Fe^{III}\{Fe^{III}(L^3)_2\}_3]$ **3**.

The results of the angular dependent magnetization measurements are shown in Fig. 8b. The magnetization data along the three crystallographic directions clearly show the easy-axis type of anisotropy (Fig. 8b). This can be concluded from the fact that the magnetization along the *z*-axis ("easy axis", shown by squares in Fig. 8b) shows a ferromagnetic-like saturation at almost $10\mu_B$ in contrast to the magnetization along the perpendicular *x*- and *y*-axes ("hard plane", depicted by the triangle and the star symbols in Fig. 8b).

We have fit the susceptibility data in the framework of a Heisenberg exchange Hamiltonian, shown in Fig. 8a by solid lines on

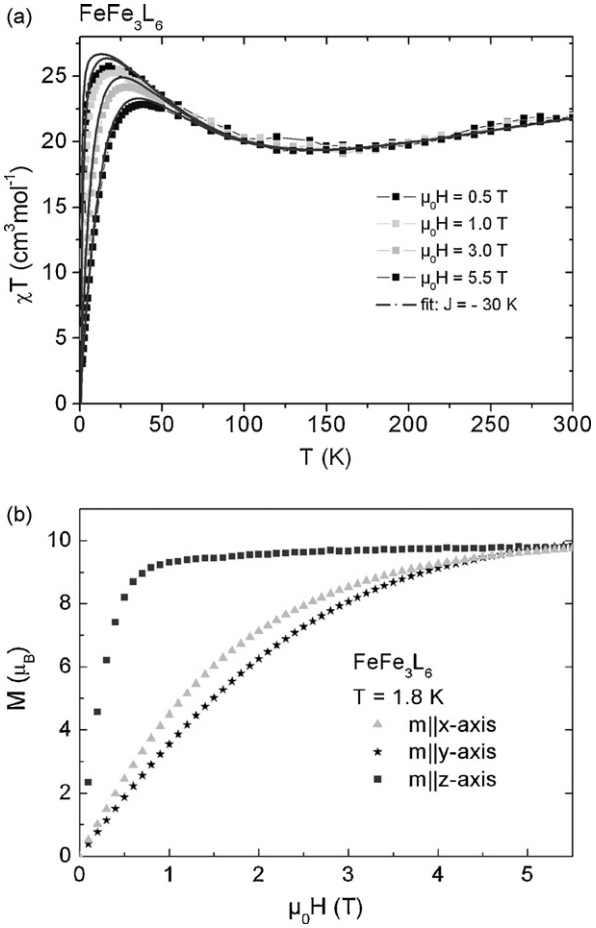


**Fig. 8.** (a) An intramolecular coupling strength $J = -30$ K has been determined for **3** by a simultaneous fit of the $\chi T$ versus $T$ curves (solid lines) using a Heisenberg Hamiltonian. The deviations at low temperature are caused by the ligand-field splitting. (b) The magnetization curves along the crystallographic *x*-, *y*- and *z*-axes show anisotropy of the easy-axis type.

top of the experimental data depicted by symbols. Thus, we were able to determine the intramolecular coupling strength (Heisenberg exchange integral) $J$ between the $Fe^{III}$ ions, having $S = 5/2$ spin. The simultaneous fit of susceptibility data measured at different magnetic field values has shown very strong antiferromagnetic coupling of peripherally located $Fe^{III}$ ions to the central $Fe^{III}$ ion with $J = -30$ K. Thus the peripheral ions do not couple magnetically to each other; therefore no ferromagnetic interaction is required to build a high-spin ground state. Having antiferromagnetic coupling between three outer $Fe^{III}$ and a central $Fe^{III}$ ion, an $S = 10/2$ ground spin state is realized in this system.

Since the excited state multiplets are lying far above the ground spin state multiplet, we can describe the magnetic properties of system **3** by a giant spin Hamiltonian:

$$H = H_{Zeeman} + H_{ligand\,field}$$

$$= g\mu_B\mu_0 SH + D(S_z{}^2 - \frac{1}{3}S(S+1)) + E(S_x{}^2 - S_y{}^2) \quad (1)$$

where $g$ is the Lande factor, $\mu_B$ is the Bohr magneton, $\mu_0$ is the vacuum permeability, $H$ is the applied magnetic field, $S_x$, $S_y$, and $S_z$ are the three components of the spin operator $S$. The parameters $D$ and $E$ define the uniaxial and the transverse anisotropy, respectively. The Hamiltonian parameters can be rather conveniently obtained when using EPR of single crystals of **3**. For this purpose, we have used a home-made EPR spectrometer, working at various microwave frequencies. Fig. 9a represents the 17.2 GHz EPR-spectra of **3** taken at different angles with respect to the applied field. In the beginning, the field was oriented along the easy axis ($\varphi = 0°$) and then the angle between the easy axis and the magnetic field was continuously changed through the hard plane ($\varphi = 90°$) up to a value of $\varphi = 180°$. We have performed EPR simulations using the Hamiltonian (1) in order to reproduce the experimental angular dependent EPR-spectra. These simulations are depicted in Fig. 9b. This way we have found a set of Hamiltonian (1) parameters, which reproduce the experiment rather well. The parameters are found to be: $D = -0.57$ K, $E = 0.056$ K [36]. They are in excellent agreement with Hamiltonian parameters, found using DFT calculations: $D_{DFT} = -0.56$ K, $E_{DFT} = 0.06$ K [35].

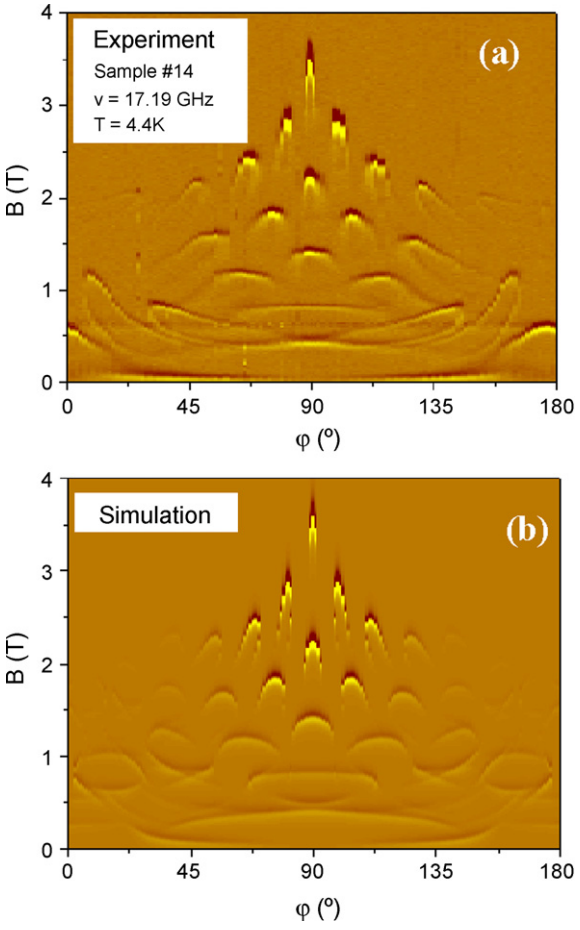


**Fig. 9.** The density plot (a) shows the measured angular dependence of EPR-spectra of **3**. The intensity of the EPR signal is given by the brown to yellow contrast. A significant change of contrast indicates an EPR peak. The theoretical density plot (b) was simulated using the Hamiltonian (Eq. (1)) with the parameter set given in the text.

Both the high-spin ground state ($S = 10/2$) and the easy-axis type of anisotropy, which is demonstrated by the measurements shown in Fig. 8b, suggest that the ferric star **3** is an SMM. The ultimate check for this would be the observation of a hysteretic behavior of the magnetization. This was done using a home-made ballistic Hall-bar magnetometer, employing 2D electron gas (2DEG) Hall sensors. Indeed, we have observed hysteresis loops typical for SMMs (Fig. 10). Additionally, we have observed another feature typical for SMMs, namely QTM, which is clearly present in the hysteresis loops. Finally, we have found that the blocking temperature of **3** is about 1.2 K. At small fields, there are additional structures in the hysteresis loops which can be explained by a weak intermolecular magnetic coupling [38].

For our STM experiments, we have deposited a solution of $[Fe^{III}\{Fe^{III}(L^1)_2\}_3]$ **3** in dichloromethane onto HOPG. We have observed various arrangements of molecules of **3** on the surface. One-dimensional chain-like arrangements were observed as a step edge decoration by molecules or by clusters of molecules, which is a well-known effect [37]. Fig. 11 summarizes different molecular arrangements, like regular arrangements of clusters of molecules (Fig. 11a), a single-molecular line (Fig. 11b), and dimer combinations (Fig. 11c). An STM topography image of a single $\{FeFe_3\}$ molecule **3** is depicted in Fig. 11d with submolecular resolution. From Fig. 11d one can see that the approximate size of the molecule is around 1.3 nm. This observation is in good agreement with X-ray data, which have shown 1.2 nm [38]. We have reproducibly obtained similar STM pictures with various samples.

As we have demonstrated by CITS spectroscopy of the grid-like complexes (see Section 3), we can expect that also in the case of **3** the level structure around the Fermi-level $E_F$ will be determined by the Fe 3d states. Hence, it can be assumed that CITS images of **3** would demonstrate predominantly a map of the Fe ions. This can be rather important for methods like spin-polarized tunneling

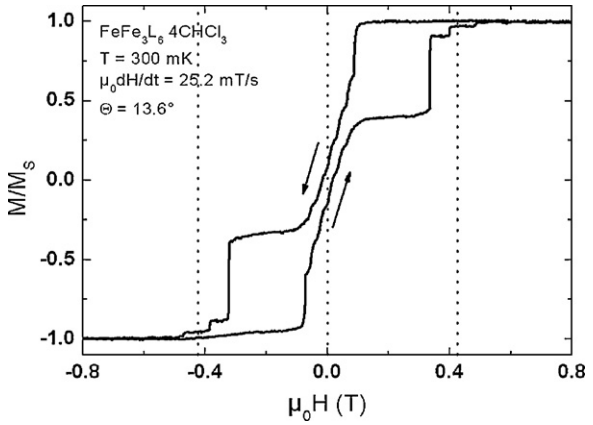


**Fig. 10.** 2DEG-Hall probe magnetization measurements of **3** show hysteresis loops. Level crossings due to ligand-field splitting at $\mu_0 H = \pm nD/(g\mu_B)$ ($n = 0$ and 1) are marked by dotted lines.

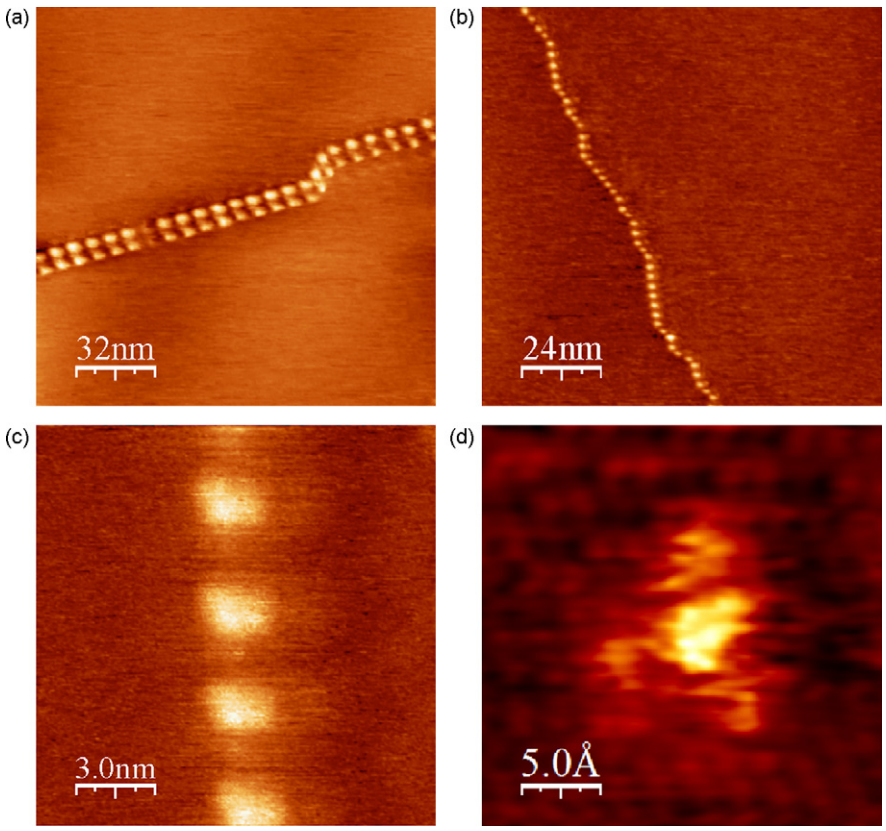


**Fig. 11.** STM results of complex **3** deposited onto a HOPG surface: (a) clusters formed from iron complexes along a graphite step. (b) A chain of single molecules. (c) Dimeric combinations of iron complexes. (d) Using a bias of −200 mV and 500 pA, an isolated molecule was mapped with submolecular resolution. The background shows the underlying graphite lattice.

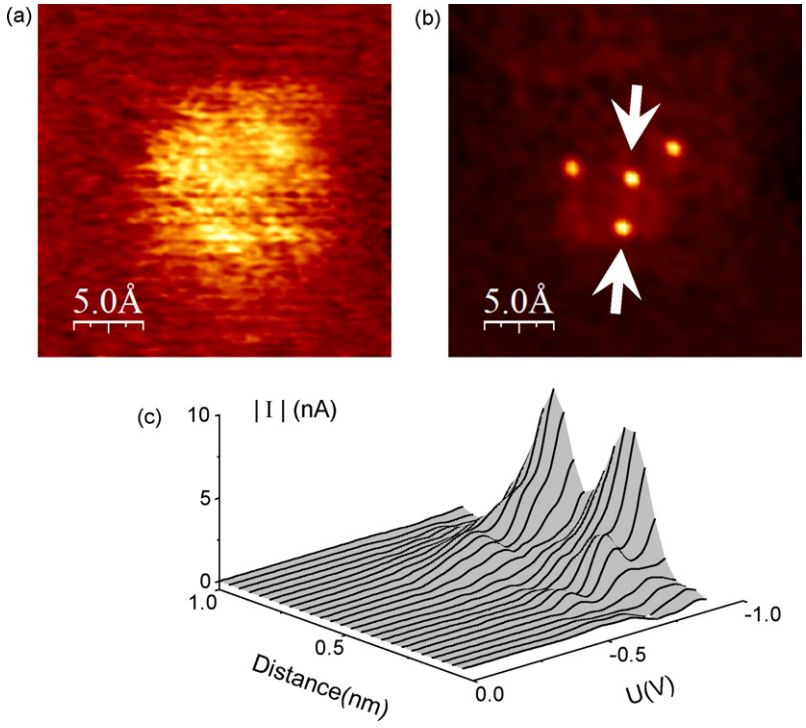


**Fig. 12.** Simultaneously recorded topography (a) and CITS current image ($V = -938$ mV) (b) of complex **3**. (c) Representation of a set of $I$–$V$ characteristics measured at 27 equidistant positions along the line between the two arrows in (b).

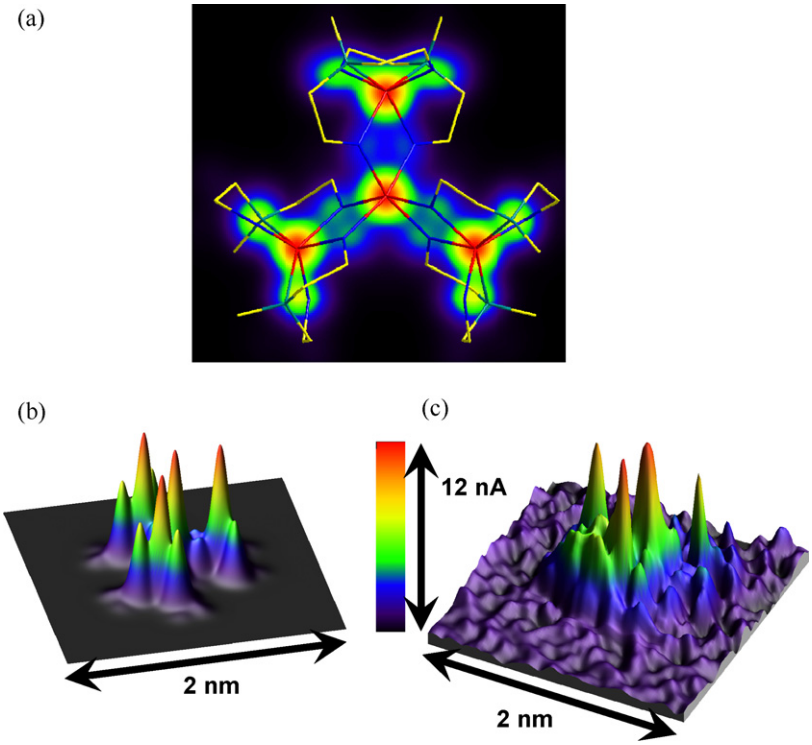


**Fig. 13.** (a) Color coded map of the DFT calculated electron density of **3** within an energy window between $E_F$ and −0.95 eV in superposition with the crystal structure data (sticks), the scale is 1.2 nm × 1.2 nm. (b) 3D representation of the DFT electron density map; (c) 3D representation of the central section of the experimental CITS map taken at −0.918 V.

[39], which are able to investigate the magnetic signature of single spin centers. As in the case of grid-like complexes, we have applied the CITS technique to molecules on HOPG substrates. As we have found in our experiments with Co and Mn centers in supramolecular [2 × 2] and [3 × 3] grid molecules that STS spectroscopy directly addresses the metal centers in rather complex molecules (see Section 3), it is reasonable to assume, that we can visualize any weakly bond metal center, i.e. we should expect to map also the star-like arrangement of Fe ions in **3**.

We depict both the constant current topographic image and the CITS current image from a single scan in Fig. 12a and b, respectively. The topographic image (Fig. 12a) shows a star-like geometry of the molecule. The diameter of the star-like arrangement in Fig. 12a is around 1.3 nm, which is very close to the outer diameter of the iron

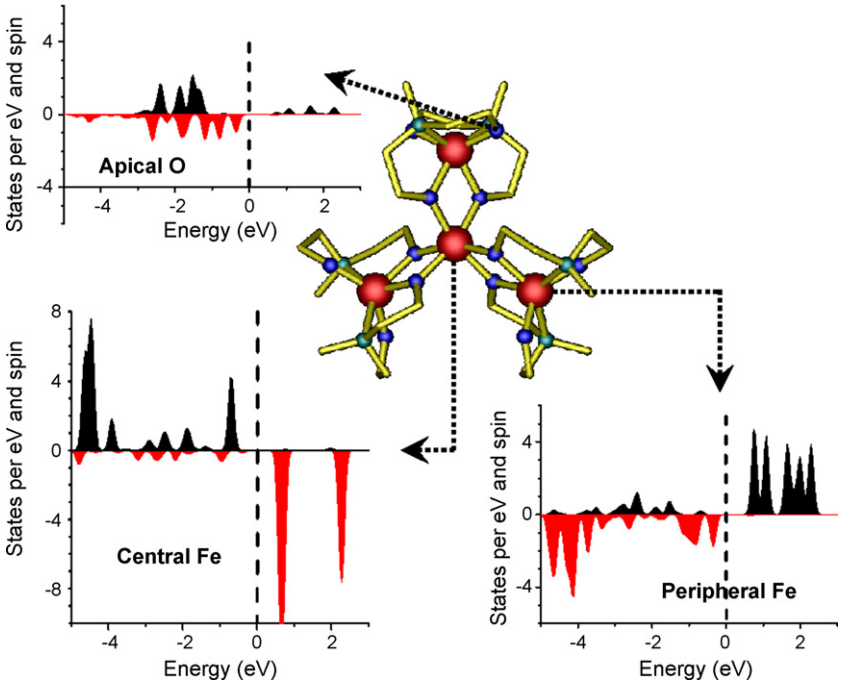


**Fig. 14.** X-ray crystal structure of **3** plotted together with the most significant local densities of states (DOS) contributing to the coordination of the Fe ions. For better comparison, all DOS curves are represented in the same scale.

"star". The CITS current map (Fig. 12b) is taken at the bias voltage of −938 mV. Unlike the topography image, it clearly shows four bright spots, which form a star-like pattern. The distances between the corresponding spots nicely match the Fe–Fe ion distances obtained from the X-ray structure studies of this molecule. The slight distortion can be ascribed to the thermal drift of the scan piezo.

In more detail the drastic increase in the *I–V* characteristics at the proposed positions of the Fe ions is depicted in Fig. 12c. Here we have plotted the full set of *I–V* curves as a function of distance for the 27 equidistant positions between the arrows in Fig. 12b. We have subtracted the background current arising from the HOPG surface. One can clearly see two peak features in Fig. 12c, which are approximately 0.3 nm apart. This perfectly matches the distances between the central and the peripheral Fe ions in the molecule. Similarly, all distances between the peaks of corresponding *I–V* curves confirm the Fe–Fe distances in the molecule. Therefore, we conclude that in our experiments we have mapped the local maxima of the DOS exactly at the positions of the Fe ions. No significant signal arising from the ligands was demonstrated in the CITS experiments presented here. This is due to their electronic levels, which are far away from the Fermi-level $E_F$ [40].

The calculated DFT local density of states of **3**, integrated from $E_F$ up to different energies, reveals the following features: as the bias voltage becomes more negative starting from zero, the peripheral $Fe^{III}$ ions yield the first signal, followed by the central $Fe^{III}$ atom at lower voltages. Additionally, we have observed much weaker features due to the apical oxygen atoms, which appear as wings close to the Fe peaks (Fig. 13a and b). This was also demonstrated in the CITS maps as a function of bias voltage. The spatial distribution of the electron density in the energy window from $E_F$ down to −0.95 eV is depicted in Fig. 13a and b. A comparison of the DFT results with the experimental observations, obtained by CITS (Fig. 13c), shows good agreement between theory and experiment.

The spin-resolved DFT calculations of the local DOS of **3** (Fig. 14) show the Fe 3d states in the region around the Fermi energy $E_F$. These states are strongly spin split and strongly hybridized with the O 2p states. The black and the red shadings in Fig. 14 show two different spin directions. The DFT calculations show a "band gap" of approximately 0.95 eV between the HOMO and the LUMO of the molecule, both of these orbitals are mostly of Fe 3d–O 2p character. Below −6 eV all the states are formed as a mixture of different orbitals which form covalent bonds and involve C 2s, 2p, N 2s, 2p states and O 2s and 2p levels [19,27]. As a major result of the spin-resolved DFT calculation we can state that the DOS landscape around the Fermi-level is solely due to the Fe 3d states. The rest of the molecule is completely transparent in the energy range ±1 eV around the Fermi-level; there are only weak contributions from the apical and bridging oxygen atoms (Fig. 14).

Moreover, the *I–V* characteristics taken along the line between two arrows depicted in Fig. 12b, show that the central Fe ion can be distinguished spectroscopically from the peripheral Fe ions, as it has a different DOS character. We found that the CITS map contains kink in the *I–V* curves at −0.57, −0.74, −0.92 V for the central ion and −0.36, −0.70, −0.87 V for the peripheral ion (Fig. 12c). This observation is in excellent agreement with the DFT DOS peaks at −0.55, −0.72, −0.91 eV for the central ion and −0.33, −0.67, −0.83 eV for the peripheral ion (Figs. 13c and 14).

## 5. Conclusions

Grid-type supramolecular assemblies, as well as star-like single-molecule magnets, are potentially useful for future molecular device architectures. Their electrochemical, magnetic and photophysical properties show that their molecular states can be changed easily. The first step towards any potential application of single magnetic molecules would be the possibility to address them properly and in a controlled way. We have shown that single grid- and star-like magnetic molecules can be attached to HOPG surfaces (a prerequisite for addressing) and self-assembled monolayers can be prepared easily. Individual molecules can be detected using surface probe techniques (STM). Submolecular resolution can be achieved by using CITS, which provides us with information about the positions of individual magnetic ions.

To summarize our experiments, we have deposited several magnetic molecules from their solutions onto HOPG. The molecules were of different structural complexity, incorporating different transition-metal ions. We have performed investigations using STM/STS and CITS under ambient conditions at room temperature. Using STM, we have estimated the dimensions of the single molecules. Our observations were in agreement with data obtained by X-ray crystallography. Using CITS measurements, recorded simultaneously with topographical information, we have measured *I–V* characteristics at each pixel of the normal STM topography. The tip to sample distance was defined by the topography parameters. We have finally obtained normal STM topography images as well as current images, extracted from the three-dimensional data set of tunneling current versus bias voltage and lateral position. The CITS investigations allowed us the localization of the positions of the incorporated transition-metal centers due to the energy-selective mapping of the local density of states. In all of our systems, the density of states near the Fermi-level was dominated by the (weakly hybridized) metal d states, which permitted us the selective mapping of the metal-ion positions, undisturbed by the surrounding organic ligands. The experimentally determined local positions of the metal ions were confirmed by first-principle DFT calculations. The SMM properties of some of our systems were characterized using single-crystal magnetometry and EPR techniques and successfully described by the giant spin Hamiltonian model.

## Acknowledgements

We thank the DFG priority program 1137 (Molecular Magnetism) and the SFB 583 (Redoxaktive Metallkomplexe) for funding to support these studies.

## References

[1] J.-M. Lehn, Supramolecular Chemistry—Concepts and Perspectives, VCH, Weinheim, 1995;
J.-M. Lehn, Macromol. Chem. Macromol. Symp. (1993) 69.
[2] P.J. Low, Dalton Trans. (2005) 2821.
[3] Ó. Paz, I. Brihuega, J.M. Gómez-Rodríguez, J.M. Soler, Phys. Rev. Lett. 94 (2005) 056103.
[4] S.D. Feyter, F.C.D. Schryver, J. Phys. Chem. B 109 (2005) 4290.
[5] S. Hembacher, F.J. Giessibl, J. Mannhart, Phys. Rev. Lett. 94 (2005) 056101.
[6] S. Novokmet, M.S. Alam, V. Dremov, F.W. Heinemann, P. Müller, R. Alsfasser, Angew. Chem. Int. Ed. 44 (2005) 803.
[7] A.M. Ako, H. Maid, S. Sperner, S.H.H. Zaidi, R.W. Saalfrank, M.S. Alam, P. Müller, F.W. Heinemann, Supramol. Chem. 17 (2005) 315.
[8] J.A. Stroscio, W.J. Kaiser (Eds.), Scanning Tunneling Microscopy, Academic Press, New York, 1993.
[9] R.J. Hamers, R.M. Tromp, J.E. Demuth, Phys. Rev. Lett. 56 (1986) 1974.
[10] M.S. Alam, S. Strömsdörfer, V. Dremov, P. Müller, J. Kortus, M. Ruben, J.-M. Lehn, Angew. Chem. Int. Ed. 44 (48) (2005) 7896.
[11] M. Rivera, R.L. Williamson, M.J. Miles, J. Vac. Sci. Technol. B 14 (1996) 1472.
[12] J. Rojo, F.J. Romero-Salguero, J.-M. Lehn, G. Baum, D. Fenske, Eur. J. Inorg. Chem. (1999) 1421.
[13] L.K. Thompson, L. Zhao, Z. Xu, D.O. Miller, W.M. Reiff, Inorg. Chem. 42 (2003) 128.
[14] R.W. Saalfrank, I. Bernt, M.M. Chowdhry, F. Hampel, G.B.M. Vaughan, Chem. Eur. J. 7 (2001) 2765.
[15] S.S. Mal, U. Kortz, Angew. Chem. Int. Ed. 44 (2005) 3777.
[16] M.S. Alam, Ph.D. Thesis, Universität Erlangen-Nürnberg, 2006.
[17] M.R. Pederson, K.A. Jackson, Phys. Rev. B 41 (1990) 7453;
K.A. Jackson, M.R. Pederson, Phys. Rev. B 42 (1990) 3276;
D.V. Porezag, M.R. Pederson, Phys. Rev. A 60 (1999) 2840;

M.R. Pederson, D.V. Porezag, J. Kortus, D.C. Patton, Phys. Stat. Solidi (B) 217 (2000) 197.
[18] http://www.uam.es/siesta;;
P. Ordejón, E. Artacho, J.M. Soler, Phys. Rev. B (1996) R10441;
J.M. Soler, E. Artacho, J.D. Gale, A. García, J. Junquera, P. Ordejón, D. Sánchez-Portal, J. Phys.: Condens. Matter 14 (2002) 2745.
[19] A. Postnikov, J. Kortus, M.R. Pederson, Phys. Stat. Solidi (B) 243 (2006) 2533.
[20] M. Ruben, J. Rojo, F.J. Romero-Salguero, L.H. Uppadine, J.-M. Lehn, Angew. Chem. Int. Ed. 43 (2004) 3644;
M. Ruben, Angew. Chem. Int. Ed. 44 (2005) 1594.
[21] P.N.W. Baxter, J.-M. Lehn, J. Fischer, M.-T. Youinou, Angew. Chem. Int. Ed. Engl. 33 (1994) 2284;
P.N.W. Baxter, J.-M. Lehn, G. Baum, D. Fenske, Angew. Chem. Int. Ed. 36 (1997) 1978;
M. Barbiou, J.-M. Lehn, J. Am. Chem. Soc. 125 (2003) 10257.
[22] M. Ruben, J.-M. Lehn, G.B.M. Vaughan, Chem. Commun. (2003) 1338.
[23] O. Waldmann, J. Hassmann, P. Müller, G.S. Hanan, D. Volkmer, U.S. Schubert, J.-M. Lehn, Phys. Rev. Lett. 78 (1997) 3390;
O. Waldmann, M. Ruben, U. Ziener, P. Müller, J.-M. Lehn, Inorg. Chem. 45 (2006) 6535.
[24] E. Breuning, M. Ruben, J.-M. Lehn, F. Renz, Y. Garcia, V. Ksenofontov, P. Gütlich, E. Wegelius, K. Rissanen, Angew. Chem. Int. Ed. 39 (2000) 2504;
M. Ruben, E. Breuning, J.-M. Lehn, V. Ksenofontov, F. Renz, P. Gütlich, G.B.M. Vaughan, Chem. Eur. J. 9 (2003) 4422;
M. Ruben, U. Ziener, J.-M. Lehn, V. Ksenofontov, P. Gütlich, G.B.M. Vaughan, Chem. Eur. J. 11 (2005) 94.
[25] M. Ruben, E. Breuning, J.-P. Gisselbrecht, J.-M. Lehn, Angew. Chem. Int. Ed. 39 (2000) 4139;
M. Ruben, E. Breuning, M. Barboiu, J.-P. Gisselbrecht, J.-M. Lehn, Chem. Eur. J. 9 (2003) 291;
D.M. Bassani, J.-M. Lehn, S. Serroni, F. Puntoriero, S. Campagna, Chem. Eur. J. 9 (2003) 5936.
[26] A. Semenov, J.P. Spatz, M. Möller, J.-M. Lehn, B. Sell, D. Schubert, C.H. Weidl, U.S. Schubert, Angew. Chem. Int. Ed. 38 (1999) 2547.
[27] M. Ruben, J.-M. Lehn, P. Müller, Chem. Soc. Rev. 35 (11) (2006) 1056.
[28] A. Semenov, J.P. Spatz, J.-M. Lehn, C.H. Weidl, U.S. Schubert, M. Möller, Appl. Surf. Sci. 144 (1999) 456.
[29] U. Ziener, J.-M. Lehn, A. Mourran, M. Möller, Chem. Eur. J. 8 (2002) 951.
[30] S. De Feyter, F.C. De Schryver, Chem. Soc. Rev. 32 (2003) 139.
[31] P. Samorí, Chem. Soc. Rev. 34 (2005) 551.
[32] V.A. Milway, S.M. Tareque Abedin, V. Niel, T.L. Kelly, L.N. Dawe, S.K. Dey, D.W. Thompson, D.O. Miller, M.S. Alam, P. Müller, L.K. Thompson, Dalton Trans. (2006) 2835;
S.K. Dey, T.S.M. Abedin, L.N. Dawe, S.S. Tandon, J.L. Collins, L.K. Thompson, A.V. Postnikov, M.S. Alam, P. Müller, Inorg. Chem. 46 (2007) 7767.
[33] R. Sessoli, D. Gatteschi, A. Caneschi, M.A. Novak, Nature 365 (1993) 141;
A.-L. Barra, A. Caneschi, A. Cornia, F. Fabrizi de Biani, D. Gatteschi, C. Sangregorio, R. Sessoli, L. Sorace, J. Am. Chem. Soc. 121 (1999) 5302;
A. Cornia, A.C. Fabretti, P. Garrisi, C. Mortal, D. Bonacchi, D. Gatteschi, R. Sessoli, L. Sorace, W. Wernsdorfer, A.-L. Barra, Angew. Chem. Int. Ed. 43 (2004)1136.
[34] A.-L. Barra, A. Caneschi, A. Cornia, F. Fabrizi de Biani, D. Gatteschi, C. Sangregorio, R. Sessoli, J. Am. Chem. Soc. 121 (1999) 5302;
D. Gatteschi, R. Sessoli, A. Cornia, Chem. Commun. (2000) 725;
A. Bouwen, A. Caneschi, D. Gatteschi, E. Goovaerts, D. Schoemaker, L. Sorace, M. Stefan, J. Phys. Chem. B 105 (2001) 2658;
A. Cornia, A.C. Fabretti, P. Garrisi, C. Mortalò, D. Bonacchi, D. Gatteschi, R. Sessoli, L. Sorace, W. Wernsdorfer, A.-L. Barra, Angew. Chem. 117 (2004) 919;
A. Cornia, A.C. Fabretti, P. Garrisi, C. Mortalò, D. Bonacchi, D. Gatteschi, R. Sessoli, L. Sorace, W. Wernsdorfer, A.-L. Barra, Angew. Chem. Int. Ed. 44 (2005) 897;
A. Takács, M. Neumann, A.V. Postnikov, K. Küpper, A. Scheurer, S. Sperner, R.W. Saalfrank, K.C. Prince, J. Chem. Phys. 124 (4) (2006) 044503.
[35] J. Kortus, M.R. Pederson, T. Baruah, N. Bernstein, C.S. Hellberg, Polyhedron 22 (2003) 1871.
[36] S. Schromm, Ph.D. Thesis, University of Erlangen-Nürnberg, 2002.
[37] R. Smoluchowski, Phys. Rev. (1941) 661.
[38] R.W. Saalfrank, A. Scheurer, I. Bernt, F.W. Heinemann, A.V. Postnikov, V. Schünemann, A.X. Trautwein, M.S. Alam, H. Rupp, P. Müller, Dalton Trans. (2006)2865.
[39] C. Iacovita, M.V. Rastei, B.W. Heinrich, T. Brumme, J. Kortus, L. Limot, J.P. Bucher, Phys. Rev. Lett. 101 (2008) 116602.
[40] Z. Klusek, W.J. Kozlowski, Electron. Spectrosc. Relat. Phenom. 107 (2000) 63.